Published in final edited form as:
Nature. 2015 February 19; 518(7539): 435–438. doi:10.1038/nature14023.

Structure of human cytoplasmic dynein-2 primed for its powerstroke

Helgo Schmidt[#], **Ruta Zalyte**[#], **Linas Urnavicius**, and **Andrew P. Carter**
Medical Research Council Laboratory of Molecular Biology, Division of Structural Studies, Francis Crick Avenue, Cambridge, CB2 0QH, United Kingdom

[#] These authors contributed equally to this work.

Abstract

Members of the dynein family, consisting of cytoplasmic and axonemal isoforms, are motors that move towards the minus ends of microtubules. Cytoplasmic dynein-1 (dynein-1) plays roles in mitosis and cellular cargo transport[1], and is implicated in viral infections[2] and neurodegenerative diseases[3]. Cytoplasmic dynein-2 (dynein-2) carries out intraflagellar transport[4] and is associated with human skeletal ciliopathies[5]. Dyneins share a conserved motor domain that couples cycles of ATP hydrolysis with conformational changes to produce movement[6-9]. Here we present the crystal structure of the human cytoplasmic dynein-2 motor bound to the ATP-hydrolysis transition state analogue ADP.vanadate (ADP.Vi)[10]. The structure reveals a closure of the motor's ring of six AAA+ domains (ATPases associated with various cellular activites: AAA1-AAA6). This induces a steric clash with the linker, the key element for the generation of movement, driving it into a conformation that is primed to produce force. Ring closure also changes the interface between the stalk and buttress coiled-coil extensions of the motor domain. This drives helix sliding in the stalk that causes the microtubule binding domain (MTBD) at its tip to release from the microtubule. Our structure answers the key questions of how ATP hydrolysis leads to linker remodelling and microtubule affinity regulation.

There are four nucleotide-binding sites in the dynein motor, but movement only depends on ATP hydrolysis in the first site (AAA1)[7,11,12]. When this site is nucleotide free or bound to ADP, the MTBD binds to the microtubule and the linker adopts the straight post-powerstroke conformation[6-8,12-14]. Upon ATP binding and hydrolysis, the MTBD detaches from the microtubule and the linker is primed into the pre-powerstroke

Correspondence and requests for materials should be addressed to A.P.C. (cartera@mrc-lmb.cam.ac.uk).

Author contributions

R.Z. and H.S. screened many dynein species for expression and crystallization. R.Z. expressed human dynein-2 in insect cells, obtained crystals in the presence of vanadate and collected data. H.S. phased the structure and built an initial model. A.P.C. built and refined the structure. R.Z. and H.S. made mutants and performed biochemical assays. L.U. performed negative stain electron microscopy. H.S., R.Z. and A.P.C. prepared the manuscript.

Supplementary information is available in the online version of the paper.

Coordinates and structure factors have been deposited in the Protein Data Bank with accession number 4RH7.

The authors declare no competing financial interests.

Europe PMC Funders Author Manuscripts

conformation[6,12,14,15] (Fig. 1a). MTBD rebinding leads to a force producing swing of the linker (powerstroke) back to the post-powerstroke position and the release of ATP hydrolysis products to reset the cycle[6,14-16].

To address how the linker is primed and dynein released from microtubules we co-crystalized the human dynein-2 motor domain with ADP.Vi to trap it in a pre-powerstroke state[6] (Extended Data Fig. 1 and Extended Data Table 1). The linker in this dynein-2:ADP.Vi structure has a 90° bend (Fig. 1b) consistent with low resolution studies of pre-powerstroke dynein[6,8,9,17]. Dynein's AAA+ domains are each divided into an α/β "large" subdomain (AAAL, helices H0-H4 and beta strands S1-S5) and an α "small" subdomain (AAAS, helices H5-H9)[16]. The individual subdomains of dynein-2:ADP.Vi are highly similar to those in post-powerstroke crystal structures of dynein-1 from *S. cerevisiae*[13] (dynein-1:APO – PDB ID: 4AKI) and *D. discoideum*[18] (dynein-1:ADP – PDB ID: 3VKG) (Extended Data Fig. 2 and Supplementary Data 1). This suggests conformational changes between these structures (Supplementary Discussion and Extended Data Fig. 3a) are not related to sequence differences but are caused by the different nucleotide states.

In dynein-2:ADP.Vi all four of nucleotide-binding sites are occupied (Fig. 1c). The AAA1 site, found between AAA+ domains AAA1 and AAA2 binds ADP.Vi (Fig. 2a and Extended Data Fig. 4a-d) via conserved motifs[19] (Fig. 2b). The trigonal-bipyramidal vanadate group mimics the ATP γ-phosphate during hydrolysis[10]. It is surrounded by three important catalytic residues[19]: the Walker B glutamate (W-B: E1742), the sensor-I asparagine (S-I: N1792) and the AAA2L arginine finger (RF: R2109), suggesting the structure is in the ATP hydrolysis competent conformation.

In the dynein-1 structures there is a gap between AAA1 and AAA2. The closure of this gap in dynein-2:ADP.Vi (Supplementary Video 1) is driven by the arginine finger-ADP.Vi contact. It is reinforced by additional interactions between AAA1L and AAA2L (Fig. 2c). A pair of conserved inserts in AAA2L[20] (the "H2 insert" and the "pre-sensor-I" (PS-I) insert) contact the H2 helix in AAA1L (Fig. 2a, c) and displace H2 and H3 relative to the rest of AAA1L (Extended Data Fig. 5a). The AAA1L sensor-I loop, which varies in position depending on dynein's nucleotide state (Extended Data Fig. 5b), swings in to contact AAA2L (Fig. 2c).

The other nucleotide-binding sites contain tightly bound nucleotides that co-purify with the motor domain (Extended Data Fig. 4e-j and Supplementary Discussion). The density in AAA2 is consistent with an ATP, as observed in all the dynein structures[13,18]. As in dynein-1:ADP, the densities in AAA3 and AAA4 suggest the presence of ADP. In the dynein-1:APO structure these sites are empty. In all dynein structures the AAA2 and AAA3 nucleotide-binding sites are in a similar closed conformation. This means that the whole AAA2-AAA4 region forms a rigid block (Extended Data Fig. 5c, d).

The linker, which is divided into four subdomains[13,18], bends between subdomains 2 and 3 in the pre-powerstroke dynein-2:ADP.Vi structure. Compared to the straight post-powerstroke linker, the mobile subdomains 1 and 2 (Link1-2, helices H5-H9) undergo a rigid-body movement relative to the static subdomains 3 and 4 (Link3-4, helices H11-H18)

(Fig. 3a and Supplementary Video 2). The hinge helix (H10), that connects Link1-2 and Link3-4, is forced to adopt a curved conformation. The isolated linker prefers a straight conformation[8] suggesting the distorted hinge helix is strained and can act as a store of energy.

In all dynein structures, the static Link3-4 is connected to the AAA+ ring via contacts to AAA1 (Extended Data Fig. 6a-c). The closure of the AAA1 site in dynein-2:ADP.Vi establishes two additional interactions (Fig. 3b). The AAA2L PS-I insert contacts the loop between H11 and H12 on Link3 via a backbone interaction. The displacement of AAA1L H2 described above, allows arginine R1726 to contact Link3 via glutamate E1420.

The mobile Link1-2 region interacts differently with the AAA+ ring in all dynein structures[13,18] (Extended Data Fig. 6d-f). In dynein-2:ADP.Vi its position is stabilized by conserved hydrophobic interactions across the linker bend (Fig. 3c and Extended Data Fig. 7). The Link1-2 region also makes two interactions with the AAA+ ring (Fig. 3d). One minor contact involves a residue (E2028) on the AAA2L H2-insert. The other, with the AAA3L H2-S3 insert, is more extensive but involves poorly conserved residues (Extended Data Fig. 7).

We had anticipated that the movement of the mobile part of the linker would be driven by its interaction with the highly conserved inserts in AAA2L[13,14,18]. It was therefore surprising to find that these inserts contact only the static part of the linker. How then could AAA1 site closure induce linker bending? To address this question we asked what would happen if the AAA+ ring adopted the ADP.Vi state but the linker remained in the straight, post-powerstroke conformation. The rigid-body behaviour of AAA2-AAA4 means that closure of the AAA1 site would lead to a steric clash between the mobile Link1-2 region and the AAA4L PS-I insert (Fig. 3e). This is demonstrated by the overlap between these regions observed in an alignment of the straight linker from dynein-1:ADP onto the dynein-2:ADP.Vi structure (Fig. 3f). The additional contacts between the AAA+ ring and the static Link3-4 (Fig. 3b) prevent it moving and mean that the clash can only be relieved by the mobile Link1-2 adopting its pre-powerstroke position (Fig. 3e, g and Supplementary Video 3).

To test this model we used negative stain electron microscopy to assay linker movement (Fig. 3h, i and Extended Data Fig. 8a, b). In the presence of ADP all dynein-2 motors had an angle between the stalk and linker of 54° +/− 13° (mean +/− SD) (Fig. 3h). In the presence of ADP.Vi the majority of motors showed a pre-powerstroke conformation with an angle of 145° +/− 20°. We then tested the ability of dynein-2 mutants to adopt the pre-powerstroke state in the presence of ADP.Vi (Fig. 3i). Removal of the AAA2L inserts abolished the linker movement, consistent with previous data[18]. It also completely prohibited microtubule gliding activity (Extended Data Fig. 8c). When the AAA4L PS-I insert was deleted only a small percentage of motors attained the pre-powerstroke conformation (Fig. 3i), supporting our model that the AAA4L PS-I insert plays a major role in linker bending. In agreement with this interpretation, the microtubule gliding velocity of this mutant was only 10% of wild type (Extended Data Fig. 8c). In contrast, removal of the Link1-2 contacts with AAA2L and AAA3L had a minimal effect on linker movement (Fig. 3i).

In addition to triggering movement of the linker, ADP.Vi binding to dynein reduces the affinity of its MTBD for microtubules[21]. Biochemical[22,23] and structural[14,18,24-26] evidence suggests this involves the helices in the stalk, coiled-coil helix 1 (CC1) and coiled-coil helix 2 (CC2), sliding past each other by one turn of α-helix. The dynein-2:ADP.Vi structure, where the MTBD has low microtubule affinity (Extended Data Fig. 9 and Supplementary Discussion), answers the key question of how the sliding is initiated.

In dynein-2:ADP.Vi the base of the stalk deviates from the symmetric, regular coiled coil observed in dynein-1:ADP (Fig. 4a). The stalk CC2 helix contains a kink, located near the stalk/buttress interface, which causes it to slip relative to CC1. The resulting asymmetry between the two helices is similar to that observed in the parallel coiled-coil homodimer Bicaudal-D[27]. A comparison of the dynein-1:ADP and dynein-2:ADP.Vi structures (Fig. 4b) suggests how the movement of the buttress, relative to the stalk, is coupled to the movement of CC2. In dynein-2:ADP.Vi the buttress slides relative to CC1 but moves together with CC2.

The stalk and buttress emerge from AAA4S and AAA5S respectively. Their relative movement is coupled to rearrangements in the AAA+ ring. Closure of the AAA1 site and the rigid body movement of AAA2-AAA4 force the AAA4/AAA5 interface to close and the AAA6L subdomain to rotate towards the ring centre (Fig. 4b and Supplementary Discussion). The AAA5S subdomain rotates as a unit together with AAA6L and this movement pulls the buttress relative to the stalk (Supplementary Videos 4 and 5).

Unlike myosin and kinesin motors, dynein shares mechanistic similarities with AAA+ proteins that remodel their substrates[28]. In dynein, one substrate is the linker which is bent by a clash with the AAA+ ring. This bent conformation is stabilized by contacts at the Link2/Link3 interface, the importance of which is highlighted by the fact that a mutation there (G1442D) can cause the human ciliopathy Jeune syndrome[5] (Supplementary Discussion). When the AAA1 site reopens the bent linker reverts to its preferred straight conformation[8] and generates force. In addition to the linker, the dynein AAA+ ring also remodels the stalk. Here the motions of AAA+ domains are directly coupled to sliding of helices in the coiled-coil (Supplementary Video 6).

Methods

Cloning of constructs

DNA sequence coding for a variant of human cytoplasmic dynein-2 isoform 1 (NCBI Reference Sequence: BAG06721) codon-optimized for expression in *Spodoptera frugiperda* (Sf9) cells, was amplified (coding region D1091-Q4307) using Phusion® High-Fidelity DNA Polymerase (New England Biolabs). The primers used for construct amplification contained sites homologous to a pFastBac vector (Invitrogen Life Science Technologies) that had been modified to contain a TEV (*tobacco etch virus)* cleavable tandem Protein A-tag for purification followed by a GFP. InFusion® (Clontech Laboratories Inc.) was used to insert the dynein-$2_{D1091-Q4307}$ gene into the pFastBac vector. The final construct used for crystallization, electron microscopy and microtubule gliding assays had an N-terminal GFP, followed by a glycine (G) serine (S) spacer and dynein-$2_{D1091-Q4307}$ (GFP-

dynein-$2_{D1091\text{-}Q4307}$). All mutants were prepared by standard cloning techniques using GFP-dynein-$2_{D1091\text{-}Q4307}$ in the pFastBac vector background as a template. ΔAAA2L H2 + PS-I had regions 2022-2030 and 2074-2085 replaced by GG, ΔAAA4L PS-I had region 2734-2774 replaced by GSGSG, ΔAAA3L H2-S3 had region 2339-2344 replaced by GG and K1413A + E2028A had K1413 and E2028 substituted by alanines. All constructs were sequence verified.

Protein expression in Sf9 cells

The modified pFastBac plasmids were transformed into a DH10 EMBacY *E. coli* strain which carried a bacmid harbouring the baculovirus genome. Clones containing bacmids in which the pFastBac vector had been successfully integrated were selected by blue white screening. Recombinant bacmids were prepared according to standard procedures, transfected into 2ml Sf9 cells ($0.5*10^6$ cells/ml) using FuGENE® HD Transfection Reagent (Promega) and incubated at 27 °C for 72h (P1 virus). 0.5 ml of P1 virus were subsequently used to infect 50 ml of Sf9 cells ($2*10^6$ cells/ml) followed by incubation at 27 °C and 127 rpm for 72h (P2 virus). 5ml of P2 virus were used to infect 500 ml of Sf9 cells ($2*10^6$ cells/ml) followed by the incubation procedure described before. Cells were harvested by centrifugation at 4 °C and 2500×g for 30 min. The pellet was washed in ice-cold PBS, snap-frozen in liquid nitrogen and stored at −80 °C.

Protein purification

Frozen pellets were resuspended in lysis buffer (30 mM HEPES pH 7.4, 50 mM KOAc, 2 mM MgOAc, 0.2 mM EGTA, 10% v/v glycerol, 300 mM KCl, 0.2 mM Mg.ATP, 1 mM DTT and 2 mM PMSF). Resuspended cells were lysed manually in a dounce homogenizer. Cell debris and insoluble proteins were removed by ultracentrifugation at 4 °C and 60000×g for 30 min. Dynein constructs were pulled out from the lysate using IgG sepharose beads (GE Healthcare, 5 ml of beads per 1l of Sf9 culture). IgG sepharose beads were washed with 15 bead volumes of lysis and TEV buffer (50mM Tris HCl pH 8, 150mM KOAc, 2 mM MgOAc, 1 mM EGTA, 10% v/v glycerol, 1 mM DTT and 0.2 mM Mg.ATP). Protein was released from the beads during overnight cleavage with TEV protease. Size-exclusion chromatography (SEC) was carried out on a Superose 6 column (GE Healthcare) in SEC buffer (20 mM Tris HCl pH 8.0, 100 mM KOAc, 2 mM MgOAc, 1 mM EGTA, 10% v/v glycerol, 1 mM DTT).

Protein crystallization

Peak fractions of GFP-dynein-$2_{D1091\text{-}Q4307}$ after SEC were pooled and concentrated to 8 mg/ml. In order to lock dynein in its pre-powerstroke state, Mg.ATP (Sigma Aldrich) and Na_3VO_4 (New England Biolabs) were added to a final concentration of 3 mM each. Crystals were obtained by hanging drop vapour diffusion at 19 °C mixing equal volumes of protein with reservoir solution (4-6 % PEG 6000 and 0.1 M Tris pH 8.0). Crystallization strictly depended on the presence of both Mg.ATP and Na_3VO_4. Crystals did not form under apo, Mg.ATP or Na_3VO_4 conditions. The crystal quality was markedly improved by microseeding. Seeds were prepared by harvesting GFP-dynein-$2_{D1091\text{-}Q4307}$ crystals into 100 µl of reservoir solution followed by vortexing with a seed bead (Jena Bioscience) for 30

Europe PMC Funders Author Manuscripts

s. After diluting the seed stock 1:10000, crystallization was carried out by mixing equal volumes of protein and seeds in reservoir solution, followed by equilibration against reservoir as described above.

Data collection and structure determination

Due to the very fragile nature of the crystals, cryoprotection was carried out in the drop by adding 1 drop volume of reservoir solution supplemented with 60 % PEG 400. After 10-30s incubation time, crystals were harvested using MicroMeshes™ (MiteGen) and flash cooled in liquid nitrogen. Heavy atom derivatization was carried out by adding solid $Na_3[PW_{12}O_{40}] \times H_2O$ (Tri-sodium phosphotungstate, Jena Bioscience) directly to the drop. After 2h incubation crystals were harvested as described above. Diffraction data was collected at 100K on beamline I02 at the Diamond Light Source. The data was integrated using MOSFLM[29] and scaled using AIMLESS[30]. In the case of the anisotropic Native-1 data set a first round of integration and scaling was carried out with a resolution limit of 3 Å. The data was then subsequently analysed with the UCLA MB Diffraction Anisotropy Server[31] (http://services.mbi.ucla.edu/anisoscale/), which suggested resolution cut-offs of a= 4.2 Å, b= 4.4 Å and c= 3.4 Å. The second round of data integration and scaling was done with the resolution cut-offs mentioned above (Extended Data Table 1). Phasing was carried out with AUTOSHARP[32] using the MIRAS (multiple isomorphous replacement with anomalous scattering) approach with a low resolution Native-2 data set and the $Na_3[PW_{12}O_{40}]$ peak and inflection data sets as heavy atom derivatives (Extended Data Table 1). The final electron density map after density modification was of sufficient quality to identify the location of all dynein-2 subdomains in the asymmetric unit. Homology models for the individual subdomains were obtained by combining PDB ID: 3VKG with the amino-acid sequence of human cytoplasmic dynein-2 isoform 1 using the PHYRE server[33]. The homology models were placed in the asymmetric unit followed by iterative rounds of refinement in REFMAC[34] against the Native-1 data set, employing the “Jelly-Body” and “secondary structure restrains” refinement options, and manual rebuilding in COOT[35]. Refining the model against the anisotropy corrected data obtained from the UCLA MB Diffraction Anisotropy Server[31] significantly improved the quality of the resulting electron density maps. The final model was evaluated by calculating a simulated annealing composite omit map in CNS[36] and had 99.9% of the residues in the allowed regions of the Ramachandran plot. All figures were prepared using PYMOL (http://www.pymol.org), LIGPLOT[37] and Jalview[38].

Vanadate mediated UV-photo cleavage of dynein-2 crystals

Crystals obtained under the conditions described above were harvested and washed 3 times in 10 µl reservoir solution followed by UV-light (254 nm) exposure for 1 h. Crystals were subsequently dissolved in sample buffer, boiled for 10 min at 95 °C and analysed by SDS-PAGE.

Nucleotide content analysis

Nucleotides were extracted from dynein-2 samples that had been purified as described above. Nucleotide extraction was carried out essentially as described previously[39]. Briefly,

concentrated protein was precipitated by adding $HClO_4$ to a final concentration of 0.5 M. The sample was vortexed and centrifuged for 10 min at 4 °C and 14000×g. The supernatant was mixed with 1M K_2HPO_4, 3M KOH and 100% acetic acid (final concentrations were 125 mM, 375 mM, and 0.5 M respectively). Total nucleotide content and protein concentration before extraction were measured using NanoDrop ND-1000 spectrophotometer.

Negative stain electron microscopy

Dynein motor domain constructs were purified as described above and diluted into EM assay buffer (50 mM Tris HCl pH 8, 150 mM KOAc, 2 mM MgOAc, 1 mM EGTA and 0.1 mM DTT) to a final concentration of 30 nM. Negative staining EM was carried out either in the presence of 3 mM Mg.ADP (+ADP) or 3 mM Mg.ATP and 3 mM Na_3VO_4 (+ADP.Vi) on plasma-cleaned carbon film on 400-square-mesh copper grids (Electron Microscopy Sciences). The samples were stained with 2% (w/v) uranyl acetate. Electron micrographs (Extended Data Fig. 8a) were recorded on a Gatan Orius SC200B CCD fitted to a FEI Tecnai G2 Spirit transmission electron microscope operating at 120 kV. Data were collected at ~1 μm underfocus, with a pixel size of 3.29 Å and an estimated dose of 20 electrons/$Å^2$ during 1s exposures. Automated particle picking was done in EMAN2.10a[40] using the Swarm boxing tool. Subsequent particle analysis was performed using RELION[41]. Autopicked particles were subjected to 2D classification to identify incorrectly picked particles which were manually checked and removed from the dataset. The remaining particles were classified into 10 classes which was sufficient to represent all observed views. Each class was then subclassified into 50 subclasses. Noisy subclasses were discarded and those remaining contained sufficient signal to noise to clearly identify the stalk and linker-GFP (Extended Data Fig. 8b). The ImageJ azimuthal average plugin (http://rsb.info.nih.gov/ij/plugins/azimuthal-average.html) was used to integrate the intensity values surrounding the outside of the motor domain with 1° bin width. This generated a plot with two peaks corresponding to the intensity for the stalk and GFP. Fitting using the sum of two Gaussian functions (Igor Pro 6.3, http://www.wavemetrics.com/products/products.html) was used to measure the angle between them. All experiments were done in triplicate. The angle distribution, using a 10° bin width, was visualised by either histogram or rose plot. The number of particles used were: WT+ADP: 3151, 9914, 7534; WT+ADP.Vi: 8710, 5793, 5284; ΔAAA2L H2 + PS-I 8664, 3408, 9220; ΔAAA4L PS-I 9835, 10799, 9955; R1413A + E2028A: 7994, 2445, 11581; ΔAAA3L H2-S3: 6535, 12185, 6399.

Microtubule gliding assays

A microtubule gliding assay was adapted from previously published work[42]. Briefly, anti-GFP antibody (Roche) was non-specifically bound to the glass surface of a flow chamber. The free surface was blocked with assay buffer (30 mM HEPES pH 7.2, 2 mM MgOAc, 1 mM EGTA, 10% (v/v) glycerol, 1 mg/ml casein and 20 μM paclitaxel). GFP-tagged dynein-2 was then applied and after 30 s incubation washed with assay buffer. Finally, motility buffer that contained microtubules, oxygen scavenging system and 1 mM ATP as an energy source was applied and gliding was observed using TIRF microscope. All data analysis was carried out with ImageJ[43].

Europe PMC Funders Author Manuscripts

Extended Data

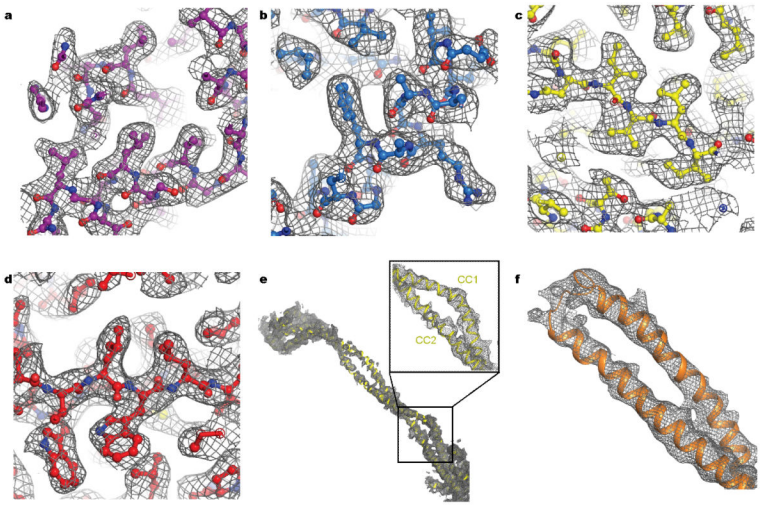

Extended Data Figure 1. Examples of the electron density quality in dynein-2:ADP.Vi

2Fo-Fc electron density in different parts of dynein-2:ADP.Vi. Amino-acid side-chains are clearly resolved in **a,** the linker, **b,** AAA1, **c,** AAA4 and **d,** AAA6. Only the main-chain could be traced in **e,** the stalk and **f,** the buttress. The electron density in **a-d** was map-sharpened. The contour level is 1σ, except for **e** which was contoured at 0.75σ.

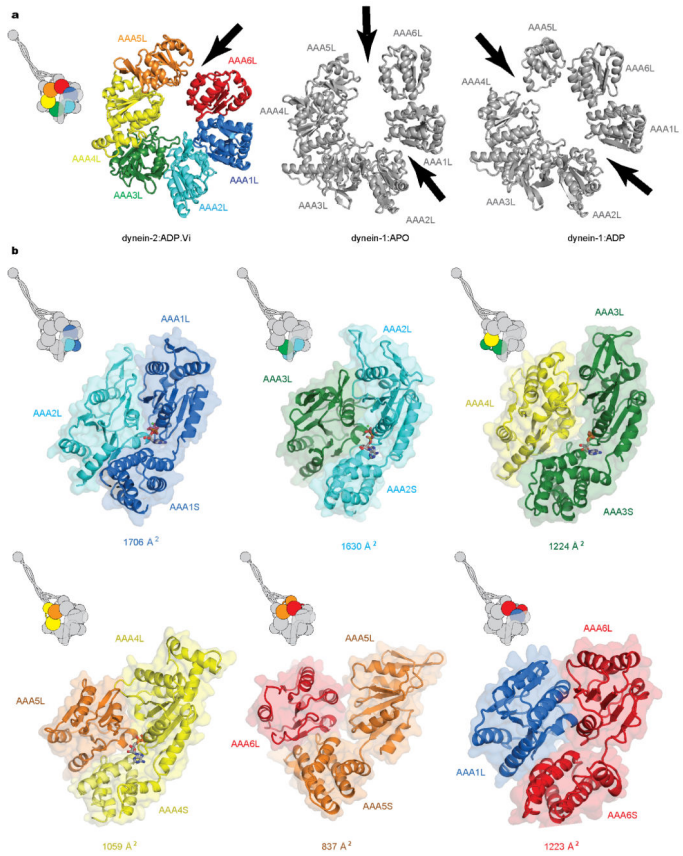

Extended Data Figure 2. Structural similarity between individual subdomains of dynein-1 and dynein-2

Alignment of individual subdomains from dynein-2:ADP.Vi and dynein-1:ADP (PDB ID: 3VKG). **a,** Alignment of AAA+ large (AAA1L-AAA6L) subdomains and the linker subdomains (Link1-2, Link3-4). **b,** Alignment of individual AAA+ small subdomains (AAA1S-AAA6S) and the C-terminal domain. Dynein-2 subdomains are coloured according to the scheme used in the main text, and shown in the inset cartoons. Dynein-1 subdomains are shown in grey. Calculated RMSD values are shown above each alignment and demonstrate that the subdomains of dynein-2 are structurally highly similar to dynein-1. The AAA+ ring subdomains with the largest RMSD differences are AAA1L and AAA1S. These subdomains are the most strongly conserved part of the dynein structure and the differences are likely due to the ADP.Vi binding. The distortion of AAA1L, by its interaction with the AAA2L inserts, was described in the main text.

Europe PMC Funders Author Manuscripts

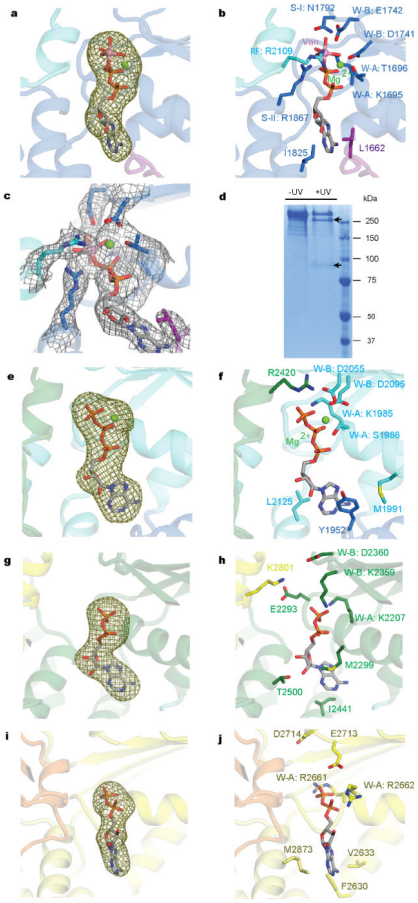

Extended Data Figure 3. Closed interfaces between AAA+ domains of the AAA+ ring in dynein-2:ADP.Vi

a, Gaps in the AAA+ rings of different dynein motor domain crystal structures. In dynein-1:APO (PDB ID: 4AKI) and dynein-1:ADP (PDB ID: 3VKG) there are gaps between AAA1L/AAA2L and AAA5L/AAA6L or AAA4L/AAA5L. In dynein-2:ADP.Vi a smaller gap exists between AAA5L/AAA6L. Gaps are indicated by black arrows. **b,** Calculated buried surface areas indicate that the interfaces between AAA1/AAA2, AAA2/AAA3, AAA3/AAA4, AAA4/AAA5 and AAA6/AAA1 are tightly closed in dynein-2:ADP.Vi (buried surface areas 1059 -1706 $Å^2$). The AAA5/AAA6 interface is more open (buried surface area 837 $Å^2$). Nucleotides are shown in stick representation. AAAL= AAA+ large subdomain, AAAS= AAA+ small subdomain.

Europe PMC Funders Author Manuscripts

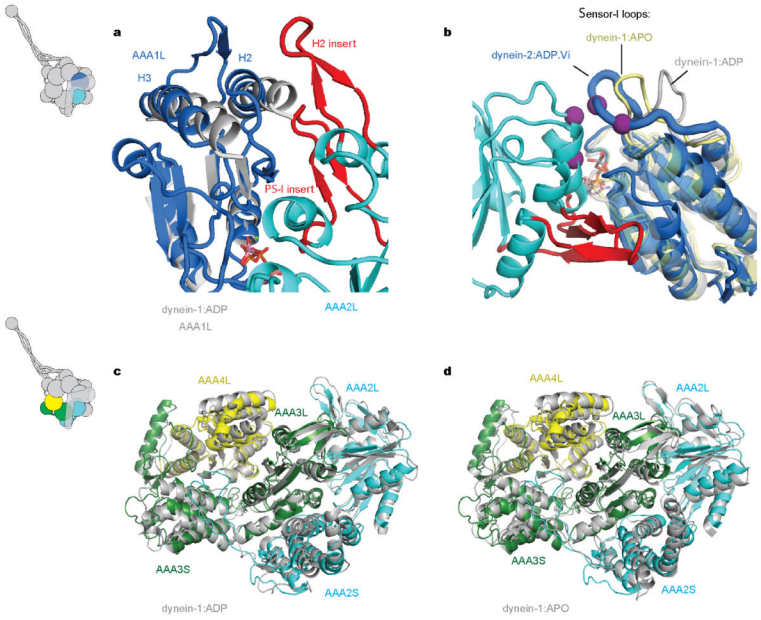

Extended Data Figure 4. The four nucleotide binding sites of dynein-2:ADP.Vi

a-c, The AAA1 site contains electron density consistent with an Mg.ADP.Vi molecule. All catalytic amino-acid residues have the correct conformation to support catalysis**. d,** Photo cleavage[11] of washed dynein-2 crystals upon exposure to UV-light (+UV) produces two bands of 300 and 90kDa (arrow heads). This suggests crystals contain an ADP.Vi group in AAA1. **e, f**, The AAA2 site contains density consistent with a Mg.ATP molecule. **g, h,** the AAA3 and **i, j,** AAA4 sites contain electron density that is best modelled as ADP. In contrast to AAA1, AAA2-AAA4 have lost the catalytic residues necessary for ATP hydrolysis (the Walker B glutamate, the arginine finger, sensor-I and sensor-II motifs). The Fo-Fc electron density (panels **a**, **e**, **g, i**) is contoured at 3σ. The 2Fo-Fc electron density (panel **c**) is contoured at 1σ. W-A: Walker A motif, W-B: Walker B motif, S-I: sensor-I, S-II: sensor-II, RF: Arginine finger. Magnesium ions (Mg^{2+}) are shown as green spheres. The vanadium ion of the vanadate molecule (Van) is shown as a pink sphere.

Europe PMC Funders Author Manuscripts

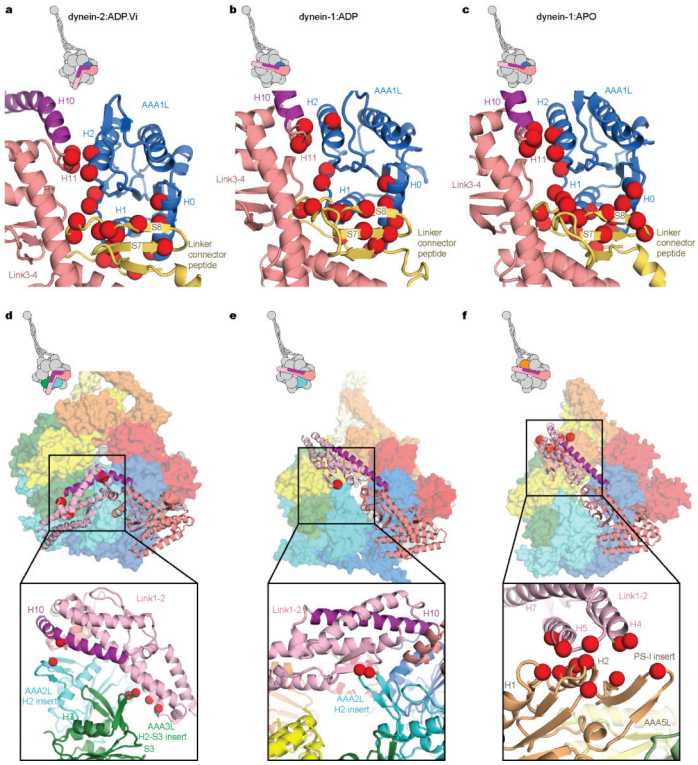

Extended Data Figure 5. Changes in conformation within dynein AAA+ ring

a, Superimposition of the AAA1L domains of dynein-2:ADP.Vi (blue) and dynein-1:ADP (grey) shows that helices H2 and H3 of AAA1L are displaced when the H2-β hairpin insert of AAA2L (red) comes into contact with H2 of AAA1L. **b,** An alignment of the AAA1L domains of dynein-2:ADP.Vi (blue), dynein-1:APO (PDB ID: 4AKI) (pale yellow) and dynein-1:ADP (PDB ID: 3VKG) (grey) shows that the loop containing the sensor-I residue is highly variable between the structures. In the presence of ADP.Vi the loop makes contacts (purple spheres) with AAA2L. **c-d,** Superimposition of AAA2-AAA4 domains between dynein-2:ADP.Vi and dynein-1:ADP (panel **c**) or dynein-1:APO (panel **d**) shows that AAA2-AAA4 move as a rigid body.

Europe PMC Funders Author Manuscripts

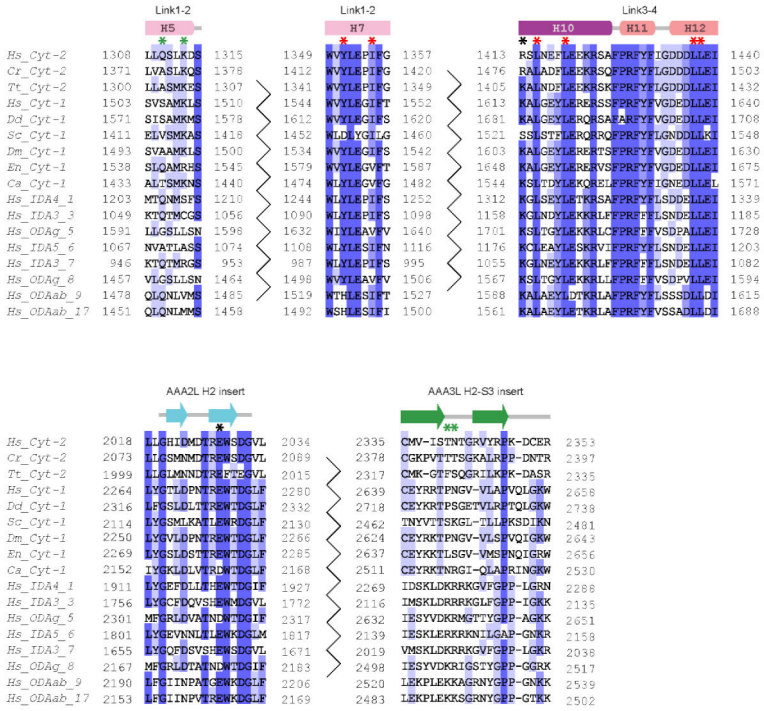

Extended Data Figure 6. Linker interaction with the AAA+ ring in dynein-2:ADP.Vi, dynein-1:ADP and dynein-1:APO

a-c, Link3-4 interacts with AAA1L in all structures similar. Mainly hydrophobic contacts exist between the linker H11 helix and the H2 helix as well as the S2 β-sheet of AAA1L. In addition the long peptide that connects the linker with AAA1 (yellow) mediates contacts between Link3-4 and AAA1L. **d,** Link1-2 is stabilised by contacts with AAA2 and AAA3 in dynein-2:ADP.Vi Link1-2, **e,** by contacts with the AAA2 H2 insert in dynein-1:ADP and **f,** by contacts with AAA5 in dynein-1:APO. Red spheres represent contacts.

Europe PMC Funders Author Manuscripts

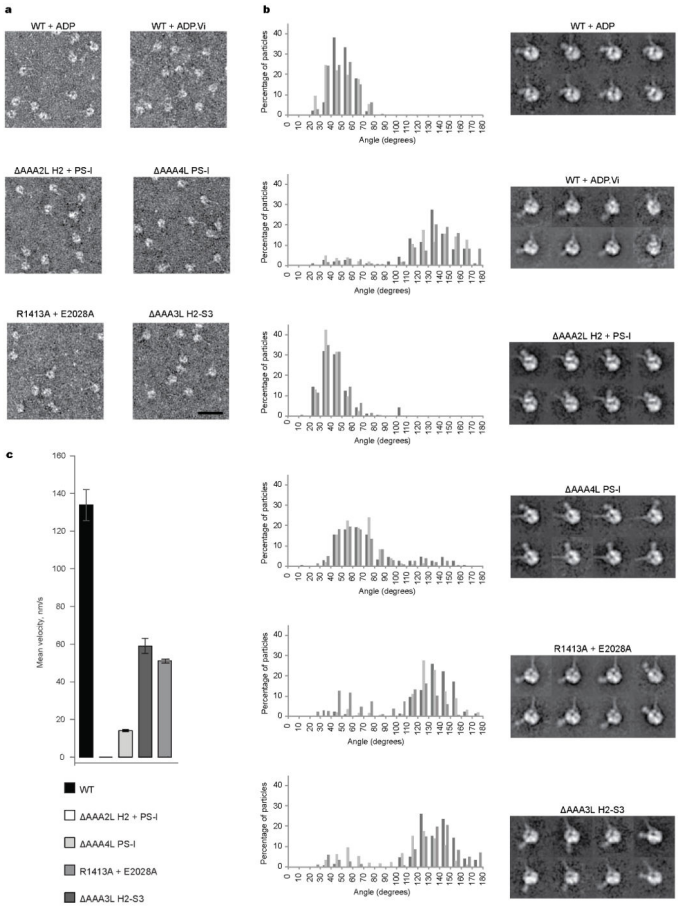

Extended Data Figure 7. Conservation of contact sites between linker and dynein ring

Multiple alignment of cytoplasmic dynein-1 (Cyt-1), dynein-2 (Cyt-2), axonemal inner arm dyneins (IDA) and outer arm γ (ODAg) and αβ (ODAab) dyneins. Dyneins are from human (Hs), *Chlamydomonas reinhardtii* (Cr), *Tetrahymena thermophila* (Tt), *Dictyostelium discoideum* (Dd), *Saccharomyces cerevisiae* (Sc), *Drosophila melanogaster* (Dm), *Emericella nidulans* (En) and *Candida albicans* (Ca). Residues are shaded by conservation, with dark blue being the most conserved. Red asterisks mark hydrophobic contacts that stabilise the bent linker conformation, black asterisks mark the contact site between AAA2L H2 insert (E2028) and the linker (R1413) and green asterisks mark poorly conserved contacts between the linker and the AAA3 H2-S3 insert.

Europe PMC Funders Author Manuscripts

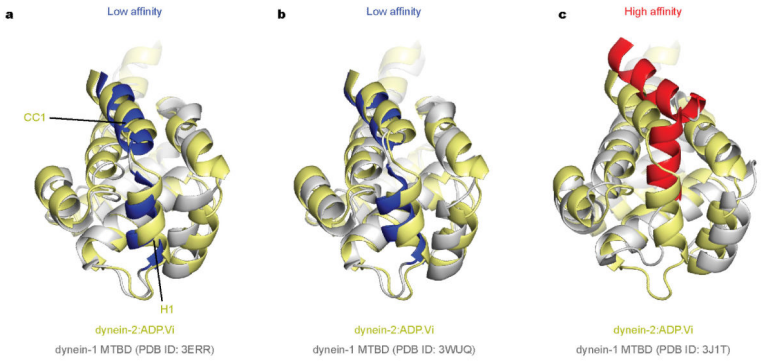

Extended Data Figure 8. Characterisation of dynein-2 mutants by negative electron microscopy and microtubule gliding assays

a, Representative micrographs showing the quality of the raw electron microscopy data. Scale bar represents 20 nm. **b,** Left – histograms showing distribution of angles between the linker and the stalk in three replicate negative stain EM experiments (10° bin width), right – representative subclasses used for angle measurement. **c,** Mean velocities of dynein-2 mutants in microtubule gliding assays. GFP-dynein-$2_{D1091\text{-}Q4307}$ (wild type: WT) glides microtubules at 134 ± 8 nm/s (N=99). The microtubule gliding velocities for the other constructs are: ΔAAA3L H2-S3: 59 ± 4 nm/s (N=79), K1413A + E2028A: 49 ± 2 nm/s (N=31) and ΔAAA4L PS-I: 14 ± 1 nm/s (N=121). Microtubule gliding was not observed in case of ΔAAA2L H2 + PS-I. Error bars represent standard error of the mean.

Europe PMC Funders Author Manuscripts

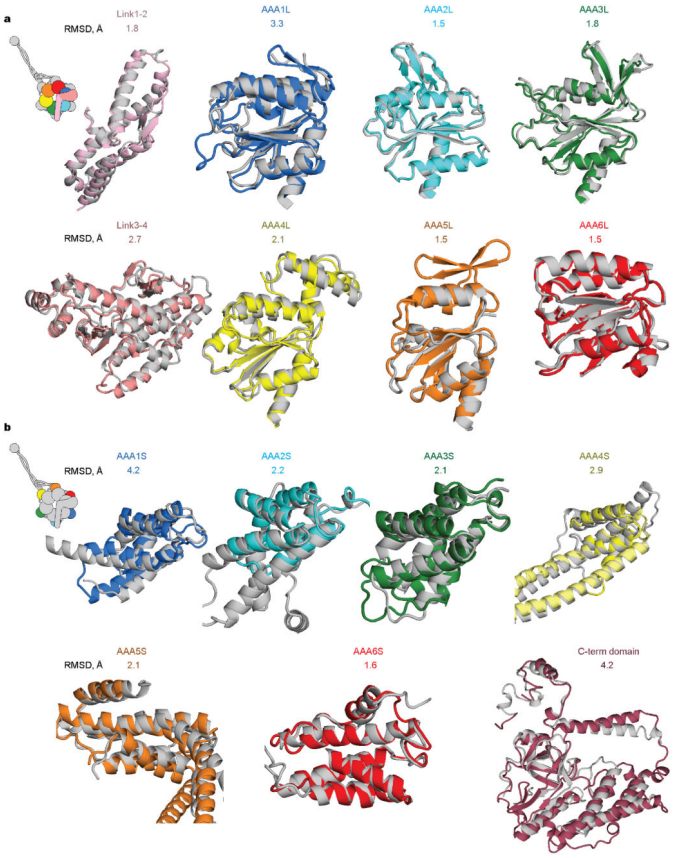

Extended Data Figure 9. The Microtubule binding domain in dynein-2 ADP.Vi is in the low microtubule affinity conformation

a, b, Alignment of dynein-2 ADP.Vi MTBD (pale yellow) with dynein-1 MTBD's (grey) in the low microtubule affinity conformation (PDB IDs: 3ERR and 3WUQ respectively), and **c,** with a dynein-1 MTBD in the high microtubule affinity conformation (PDB ID: 3J1T). The stalk CC1 and the MTBD H1 undergo conformational changes depending on the microtubule affinity of the MTBD. In dynein-2:ADP.Vi the arrangement of these structural elements suggests the MTBD is in the low microtubule affinity conformation. Stalk CC1 and MTBD H1 are coloured blue in low affinity structures and red in high affinity structures.

Europe PMC Funders Author Manuscripts

Europe PMC Funders Author Manuscripts

Extended Data Table 1

Data collection, phasing and refinement statistics.

Dataset	**Native-1**	**Native-2**	**$Na_3[PW_{12}O_{40}]$**	
Space group	$C222_1$	$C222_1$	$C222_1$	
Cell dimensions				
a, *b*, *c* (Å)	136.0, 487.2, 276.5	136.2, 487.7, 276.9	135.7, 481.9, 276.5	
			Peak	*Inflection*
Wavelength (Å)	0.97949	0.97949	1.21416	1.21476
Resolution (Å)	56.5-3.40	56.1-6.0	65.9-6.0	69.5-6.0
R_{sym} Or R_{merge}	10.1 (69.2)*	6.3 (17.7)	24.0 (111.6)	36.1 (170.6)
$I/\sigma I$	7.6 (1.1)	207.2 (28.4)	8.0 (2.4)	5.9 (1.7)
Completeness (%)	62.2 (1.9)§	94.9 (99.6)	99.8 (99.9)	99.8 (100.0)
Redundancy	4.1	3.6	11.7	10.0
Refinement				
Resolution (Å)	56.6-3.41			
No. reflections	74060			
R_{work}/ R_{free}	23.7/28.5			
No. atoms	22816			
Protein	22697			
Ligand/ion	119			
Water	-			
B-factors				
Protein	122.0			
Ligand/ion	69.8			
Water	-			
R.m.s deviations				
Bond lengths (Å)	0.012			
Bond angles (°)	1.55			

*Highest resolution shell is shown in parenthesis.

§The low completeness to 3.4 Å is due to the anisotropic diffraction limits (*a*= 4.2 Å, *b*= 4.4 Å, *c*= 3.4 Å). When the data is scaled to a resolution limit of 4.2 Å the overall completeness is 97.9% and the completeness in the highest resolution shell is 78.4%.

Supplementary Material

Refer to Web version on PubMed Central for supplementary material.

Acknowledgments

This work was funded by the Medical Research Council, UK (MC_UP_A025_1011), a Wellcome Trust New Investigator Award (WT100387) and an EMBO Young Investigator Award. We thank M. Yu for in house support with X-ray data collection and Diamond Light Source for access to beamline I02 (MX8547-70). We thank G. Dornan and M. Barczyk for assistance with insect cell culture. We also thank S. Bullock and D. Barford for their advice and comments on the manuscript.

References

1. Roberts AJ, Kon T, Knight PJ, Sutoh K, Burgess SA. Functions and mechanics of dynein motor proteins. Nat Rev Mol Cell Biol. 2013; 14:713–726. [PubMed: 24064538]
2. Dodding MP, Way M. Coupling viruses to dynein and kinesin-1. EMBO J. 2011; 30:3527–3539. [PubMed: 21878994]
3. Schiavo G, Greensmith L, Hafezparast M, Fisher EM. Cytoplasmic dynein heavy chain: the servant of many masters. Trends Neurosci. 2013; 36:641–651. [PubMed: 24035135]
4. Ishikawa H, Marshall WF. Ciliogenesis: building the cell's antenna. Nat Rev Mol Cell Biol. 2011; 12:222–234. [PubMed: 21427764]
5. Schmidts M, et al. Exome sequencing identifies DYNC2H1 mutations as a common cause of asphyxiating thoracic dystrophy (Jeune syndrome) without major polydactyly, renal or retinal involvement. J Med Genet. 2013; 50:309–323. [PubMed: 23456818]
6. Burgess SA, Walker ML, Sakakibara H, Knight PJ, Oiwa K. Dynein structure and power stroke. Nature. 2003; 421:715–718. [PubMed: 12610617]
7. Kon T, Mogami T, Ohkura R, Nishiura M, Sutoh K. ATP hydrolysis cycle-dependent tail motions in cytoplasmic dynein. Nat Struct Mol Biol. 2005; 12:513–519. [PubMed: 15880123]
8. Roberts AJ, et al. ATP-driven remodeling of the linker domain in the dynein motor. Structure. 2012; 20:1670–1680. [PubMed: 22863569]
9. Roberts AJ, et al. AAA+ Ring and linker swing mechanism in the dynein motor. Cell. 2009; 136:485–495. [PubMed: 19203583]
10. Davies DR, Hol WG. The power of vanadate in crystallographic investigations of phosphoryl transfer enzymes. FEBS Lett. 2004; 577:315–321. [PubMed: 15556602]
11. Gibbons IR, Gibbons BH, Mocz G, Asai DJ. Multiple nucleotide-binding sites in the sequence of dynein beta heavy chain. Nature. 1991; 352:640–643. [PubMed: 1830927]
12. Kon T, Nishiura M, Ohkura R, Toyoshima YY, Sutoh K. Distinct functions of nucleotide-binding/hydrolysis sites in the four AAA modules of cytoplasmic dynein. Biochemistry. 2004; 43:11266–11274. [PubMed: 15366936]
13. Schmidt H, Gleave ES, Carter AP. Insights into dynein motor domain function from a 3.3-A crystal structure. Nat Struct Mol Biol. 2012; 19:492–497. S491. [PubMed: 22426545]
14. Carter AP. Crystal clear insights into how the dynein motor moves. J Cell Sci. 2013; 126:705–713. [PubMed: 23525020]
15. Imamula K, Kon T, Ohkura R, Sutoh K. The coordination of cyclic microtubule association/dissociation and tail swing of cytoplasmic dynein. PNAS USA. 2007; 104:16134–16139. [PubMed: 17911268]
16. Carter AP, Cho C, Jin L, Vale RD. Crystal structure of the dynein motor domain. Science. 2011; 331:1159–1165. [PubMed: 21330489]
17. Lin J, Okada K, Raytchev M, Smith MC, Nicastro D. Structural mechanism of the dynein power stroke. Nat Cell Biol. 2014; 16:479–485. [PubMed: 24727830]
18. Kon T, et al. The 2.8 A crystal structure of the dynein motor domain. Nature. 2012; 484:345–350. [PubMed: 22398446]

19. Wendler P, Ciniawsky S, Kock M, Kube S. Structure and function of the AAA+ nucleotide binding pocket. Biochim Biophys Acta. 2012; 1823:2–14. [PubMed: 21839118]
20. Gleave ES, Schmidt H, Carter AP. A structural analysis of the AAA+ domains in Saccharomyces cerevisiae cytoplasmic dynein. J Struct Biol. 2014; 186:367–375. [PubMed: 24680784]
21. Vale RD, Soll DR, Gibbons IR. One-dimensional diffusion of microtubules bound to flagellar dynein. Cell. 1989; 59:915–925. [PubMed: 2531633]
22. Gibbons IR, et al. The affinity of the dynein microtubule-binding domain is modulated by the conformation of its coiled-coil stalk. J Biol Chem. 2005; 280:23960–23965. [PubMed: 15826937]
23. Kon T, et al. Helix sliding in the stalk coiled coil of dynein couples ATPase and microtubule binding. Nat Struct Mol Biol. 2009; 16:325–333. [PubMed: 19198589]
24. Carter AP, et al. Structure and functional role of dynein's microtubule-binding domain. Science. 2008; 322:1691–1695. [PubMed: 19074350]
25. Nishikawa Y, et al. Structure of the entire stalk region of the Dynein motor domain. J Mol Biol. 2014; 426:3232–3245. [PubMed: 25058684]
26. Redwine WB, et al. Structural basis for microtubule binding and release by dynein. Science. 2012; 337:1532–1536. [PubMed: 22997337]
27. Liu Y, et al. Bicaudal-D uses a parallel, homodimeric coiled coil with heterotypic registry to coordinate recruitment of cargos to dynein. Genes Dev. 2013; 27:1233–1246. [PubMed: 23723415]
28. Erzberger JP, Berger JM. Evolutionary relationships and structural mechanisms of AAA+ proteins. Annu Rev Biophys Biomol Struct. 2006; 35:93–114. [PubMed: 16689629]
29. Battye TG, Kontogiannis L, Johnson O, Powell HR, Leslie AG. iMOSFLM: a new graphical interface for diffraction-image processing with MOSFLM. Acta Crystallogr D Biol Crystallogr. 2011; 67:271–281. [PubMed: 21460445]
30. Evans P. Scaling and assessment of data quality. Acta crystallographica. Section D, Biological crystallography. 2006; 62:72–82.
31. Strong M, et al. Toward the structural genomics of complexes: crystal structure of a PE/PPE protein complex from Mycobacterium tuberculosis. PNAS USA. 2006; 103:8060–8065. [PubMed: 16690741]
32. Vonrhein C, Blanc E, Roversi P, Bricogne G. Automated structure solution with autoSHARP. Methods Mol Biol. 2007; 364:215–230. [PubMed: 17172768]
33. Kelley LA, Sternberg MJ. Protein structure prediction on the Web: a case study using the Phyre server. Nat Protoc. 2009; 4:363–371. [PubMed: 19247286]
34. Murshudov GN, et al. REFMAC5 for the refinement of macromolecular crystal structures. Acta Crystallogr D Biol Crystallogr. 2011; 67:355–367. [PubMed: 21460454]
35. Emsley P, Cowtan K. Coot: model-building tools for molecular graphics. Acta Crystallogr D Biol Crystallogr. 2004; 60:2126–2132. [PubMed: 15572765]
36. Brunger AT, et al. Crystallography & NMR system: A new software suite for macromolecular structure determination. Acta Crystallogr D Biol Crystallogr. 1998; 54:905–921. [PubMed: 9757107]
37. Wallace AC, Laskowski RA, Thornton JM. LIGPLOT: a program to generate schematic diagrams of protein-ligand interactions. Protein Eng. 1995; 8:127–134. [PubMed: 7630882]
38. Waterhouse AM, Procter JB, Martin DM, Clamp M, Barton GJ. Jalview Version 2 - a multiple sequence alignment editor and analysis workbench. Bioinformatics. 2009; 25:1189–1191. [PubMed: 19151095]
39. Huecas S, Andreu JM. Energetics of the cooperative assembly of cell division protein FtsZ and the nucleotide hydrolysis switch. J Biol Chem. 2003; 278:46146–46154. [PubMed: 12933789]
40. Tang G, et al. EMAN2: an extensible image processing suite for electron microscopy. J Struct Biol. 2007; 157:38–46. [PubMed: 16859925]
41. Scheres SH. RELION: implementation of a Bayesian approach to cryo-EM structure determination. J Struct Biol. 2012; 180:519–530. [PubMed: 23000701]
42. Reck-Peterson SL, et al. Single-molecule analysis of dynein processivity and stepping behavior. Cell. 2006; 126:335–348. [PubMed: 16873064]

43. Schneider CA, Rasband WS, Eliceiri KW. NIH Image to ImageJ: 25 years of image analysis. Nat Methods. 2012; 9:671–675. [PubMed: 22930834]

Europe PMC Funders Author Manuscripts

Europe PMC Funders Author Manuscripts

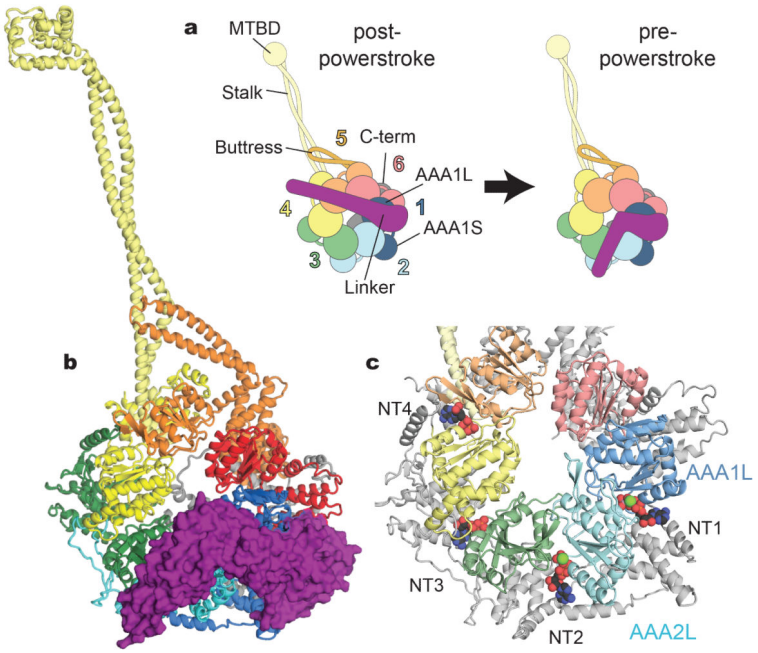

Figure 1. Crystal structure of dynein-2:ADP.Vi

a, Schematic representation of a dynein motor domain in post- and pre-powerstroke states. Structural elements are labelled and colour-coded. AAA+ domains (1-6) consist of large (AAAL) and small (AAAS) subdomains. The coiled-coil stalk is supported by the coiled-coil buttress and harbours the microtubule binding domain (MTBD). A C-terminal domain (C-term) runs underneath the AAA+ ring. **b,** Overview of dynein-2:ADP.Vi in cartoon/surface representation. The linker features a 90° bend. **c**, Nucleotides (NT1-NT4, sphere representations) are mainly bound between AAA+ large domains (colour-coded). AAA1L and AAA2L form the important AAA1 nucleotide-binding site.

Europe PMC Funders Author Manuscripts

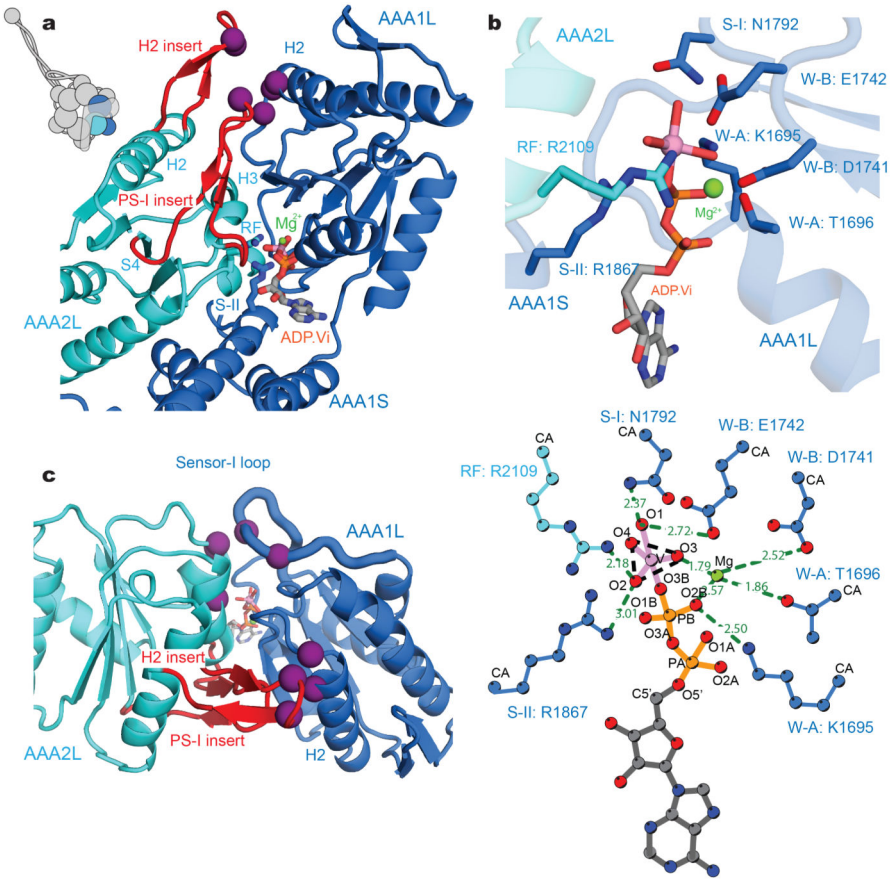

Figure 2. ADP.Vi binding to AAA1 nucleotide-binding site induces closure of AAA1/AAA2 interface

a, AAA1L, AAA1S and AAA2L enclose ADP.Vi. The AAA2L H2 and PS-I inserts (red) contact AAA1L H2. **b,** Upper panel: The Mg^{2+}.ADP contacts the Walker A (W-A:K1695), Walker B (W-B:D1741) and the sensor-II (S-II:R1867) residues. The trigonal-bipyramidal Vi-group mimicks the ATP-hydrolysis transition state and is surrounded by sensor-I (S-I:N1792) and Walker B (W-B:E1742) residues and the AAA2L arginine finger (RF). Lower panel: Schematic diagram showing the distances from ADP.Vi to the catalytic residues. **c,** AAA1/AAA2 interface closure is reinforced by the AAA1L sensor-I loop contacting AAA2L. Purple spheres represent contacts.

Europe PMC Funders Author Manuscripts

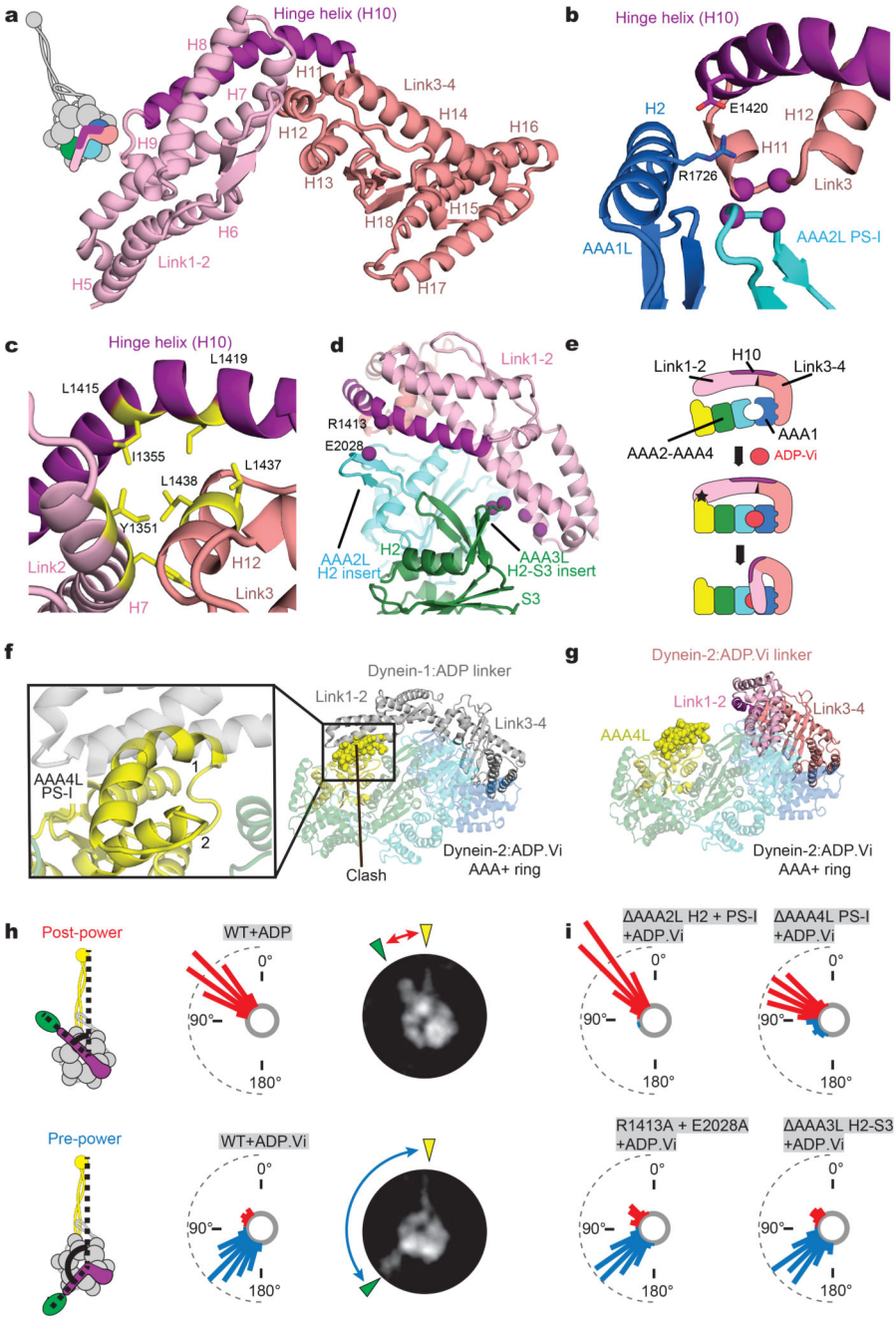

Figure 3. Linker bending upon closure of AAA1 nucleotide-binding site

a, A 90° bend between linker subdomains 1&2 (Link1-2) and 3&4 (Link3-4) forces the hinge helix (H10) to curve. **b,** The AAA2L PS-I insert contacts Link3 and AAA1L R1726 forms a saltbridge with E1420 on the hinge helix. **c**, Hydrophobic residues (yellow) stabilize the Link2/Link3 bend. **d,** Link1-2 contacts the AAA2:H2 and AAA3L:H2-S3 inserts. **e,** AAA1 site (blue/cyan) closure causes a rigid-body movement of AAA2-AAA3-AAA4 (cyan-green-yellow) leading to a clash (black star) with Link1-2 (lightpink). To relieve the clash, the linker adopts the pre-powerstroke conformation. **f,** The straight post-powerstroke

linker (grey), aligned via Link3-4 onto dynein-2:ADP.Vi, would clash with the AAA4L PS-I insert (yellow spheres). **g,** In dynein-2:ADP.Vi the linker moved to avoid the clash. **h,** In a negative stain electron microscopy assay the angle between the stalk (yellow) and GFP-linker (green/purple) of the dynein-2:ADP motor is 54°+/−13° (mean +/− SD). With ADP.Vi most dynein-2 motors are in a pre-powerstroke state with an angle of 145°+/−20° (mean +/− SD). **i,** Deletion of the AAA2L (ΔAAA2L:H2+PS-I) or AAA4L inserts (ΔAAA4L:PS-I) hinders the linker adopting the pre-powerstroke conformation with ADP.Vi. Mutation of either AAA3 (ΔAAA3L:H2-S3) or AAA2 (R1413A+E2028A) linker-ring contacts, has no effect. The dashed half-circles in panels **h** and **i** mark 20% dynein-2 particles.

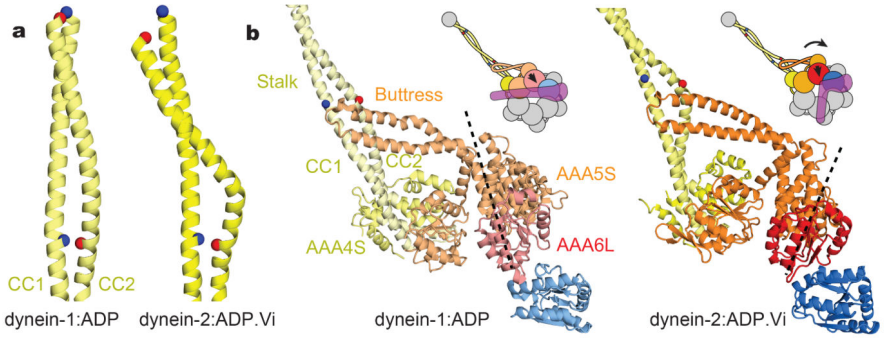

Figure 4. Buttress movement triggers helix sliding in the stalk

a, In dynein-2:ADP.Vi the stalk CC2 is kinked. Compared to the dynein-1:ADP stalk, CC2 is displaced by one turn of α-helix relative to CC1. Blue and red spheres represent equivalent amino-acid residues in the two structures. **b,** The two stalk conformations are stabilized by movement of the buttress, which slips relative to CC1, but moves with CC2 when comparing the two structures. The buttress movement is the result of a rotation of the AAA6L/AAA5S unit (shown by the position of the dashed black line).

Europe PMC Funders Author Manuscripts